DOI: 10.1002/ ((please add manuscript number))

Article type: Full Paper

Ultralow-strain Zn-substituted Layered Oxide Cathode with Suppressed P2-O2 Transition for Stable Sodium Ion Storage

Yanxia Wang[†], Liguang Wang[†], He Zhu, Jun Chu, Yongjin Fang, Lina Wu, Ling Huang, Yang Ren, Cheng-Jun Sun, Qi Liu*, Xinping Ai, Hanxi Yang, Yuliang Cao*

Y.-X. Wang, J. Chu, Dr. Y.-J. Fang, Prof. X.-P. Ai, Prof. H.-X Yang, Prof. Y.-L Cao College of Chemistry and Molecular Sciences, Hubei Key Laboratory of Electrochemical Power Sources, Wuhan University, Wuhan 430072, P. R. China Email: ylcao@whu.edu.cn

Dr. L.-G. Wang, Dr. H. Zhu, Dr. Q. Liu, Department of Physics, City University of Hong Kong, Hong Kong 999077, P. R. China

Email: qiliu63@cityu.edu.hk

Dr. L.-N. Wu, Prof. L. Huang

College of Chemistry and Chemical Engineering, Xiamen University, Xiamen 361005, P. R. China

Dr. Y. Ren, Dr. C.-J. Sun

X-ray Science Division, Argonne National Laboratory, Illinois 60439, United States Dr. Q. Liu

Shenzhen Research Institution, City University of Hong Kong, Shenzhen 518057, P. R. China

⁺ These authors contributed equally to this work.

Keywords: ultralow strain, substitution, phase transition, sodium ion batteries

Layered transition metal oxides have drawn much attention as a promising candidate cathode materials for sodium-ion batteries. However, their performance degradation originated from strains and lattice phase transitions remains a critical challenge. Herein, a high-concentration Zn-substituted Na_xMnO₂ cathode with strongly suppressed P2-O2 transition is investigated, which exhibiting as low as 1.0% volume change in the charge/discharge process. Such ultralow strain characteristic ensures a stable host for

sodium ion storage, which significantly improves the cycling stability and rate capability of the cathode material. Also, the strong coupling between the highly reversible capacity and the doping content of Zn in Na_xMnO₂ is investigated. It is suggested that reversible anionic redox reaction can be effectively triggered by Zn ions and also highly dependent on the Zn content. Such an ion doping strategy could shed light on the design and construction of stable and high-capacity sodium ion host.

1. Introduction

Sodium-ion batteries (SIBs) are now actively developed as a low cost alternative to Li ion batteries for large-scale electric energy storage due to the rich abundance and low cost of sodium resources. Tremendous efforts have been made to explore suitable cathode and anode materials electrodes. However, akin to their lithium counterparts, SIBs are currently hampered by the capacity-limited cathode materials that usually fail to provide sufficient active sites for reversible Na⁺ (de)intercalation. Unlike the much smaller Li⁺ ions (0.76 Å), the insertion of larger Na⁺ ions (1.02 Å) would induce remarkable volume change and complicated phase transitions of the host materials, leading to structural collapse and the consequent severe capacity decay of the electrodes. Therefore, developing high performance cathode materials with low strain and weak phase transition remains a critical challenge for the commercial development of SIBs.

To date, layered transition metal oxides, Na_xMO₂ (where M refers to transition metals), are generally recognized as preferable SIB cathodes owing to their open framework, low cost, high theoretical capacity and facile synthesis. [12] Among them, Na_xMnO₂ stands out as a leading candidate especially due to its unique structural diversity that enables a flexible choice to host Na⁺. The crystal structure of Na_xMnO₂ is highly correlated to the Na/Mn ratio (i.e., 2/3, 1), and two typical type structures (P2 and O3) which are defined by the different MnO₂-slab stacking along c-direction are most comprehensively investigated. [13] Here, the terms of "P" and "O" represent the prismatic and octahedral ligand environment of Na⁺, respectively, and the following numbers indicate the repeated folds of MnO₂ layers in a unit cell. Typically, both twotype Na_xMnO₂ frameworks undergo complicated phase transitions during sodium insertion/extraction processes, arising from the Jahn-Teller distortion of high spin Mn^{III} $(t_{2g}^{3}e_{g}^{1})$. [14, 15] More seriously, such distortion could further cause large cell volume change and lattice strain. [16, 17] Compared to the O3 structure, the P2 type Na_{2/3}MnO₂ is generally expected to exhibit better stability with less distorted Mn^{3+} , but it still suffers from an undesirable P2-O2 phase transition and subsequent MnO2 slab gliding at high voltage region, leading to a huge volume change of 15-20%. [18] Such a large mechanical strain is the dominant cause for the structural degradation and capacity decay of the layered Na_xMnO₂ cathode.

In order to maintain stable electrochemical performance, great efforts have been made towards improving the long-term structural integrity of Na_{2/3}MnO₂ through ionic doping technique^[19-27]. For example, Hu and co-workers reported a P2-type

 $Na_{0.72}[Li_{0.24}Mn_{0.76}]O_2$, which demonstrates a considerable reversible capacity and a very low volume change of 3.34% during cycles.^[28] To proceed a further step forward, it is much desirable to completely eliminate the unexpected phase transitions (especially the P2-O2 phase transition) so as to significantly reduce the mechanical strain of the host Na_xMnO_2 materials.

In this work, we develop a Zn-doping strategy to suppress the unwanted irreversible P2-O2 phase transitions. By simply controlling the doping amount of Zn, the Zn-substituted Na_xMnO₂ cathode can deliver a high initial capacity over 200 mAh g⁻¹ cycled in 4.5-1.5 V. *In situ* synchrotron high-energy X-ray diffraction (HEXRD) technique clearly demonstrates that the undesired P2-O2 phase transition has been greatly suppressed during operations with the unit cell volume change as small as 1.0%. Benefiting from the suppressed lattice strain, the Zn-substituted Na_xMnO₂ electrode demonstrates a superior structural stability during the sodium insertion reaction and therefore a greatly enhanced cyclability. Also, multiple X-ray spectroscopic analysis reveals that this highly reversible capacity arises from oxygen redox activity, which correlates closely with the Zn content. We believe such an ion-doping strategy can be easily adopted to a wide range of layered Na⁺ insertion cathodes to suppress the phase transitions and therefore to stabilize the host structure for developing cycle-stable SIBs.

2. Results and Discussion

2.1. Physical Characterizations

The Na_{2/3}Zn_{1/4}Mn_{3/4}O₂ (denoted as NZM) material was obtained by doping one quarter of Zn ions at Mn sites in the typical P2-type Na_{2/3}MnO₂ (denoted as NM). The chemical compositions of the materials were determined by inductively coupled plasma-atomic emission spectroscopic (ICP-AES) as listed in Table S1. Except for minute quantity of sodium loss during high temperature calcination, both the chemical compositions of NZM and NM are very close to the expectations. Thus, the oxidation states of Mn ions in NZM and NM are estimated to be +3.83 and +3.36, respectively. According to the ex situ HE-XRD results (Figure 1a and Figure S1), both the NZM and NM materials can be indexed to the P2 structure (Space group: P63/mmc). The refined structure of NZM as shown in Table S2 demonstrates that the Zn ions are occupied at the Mn site (Wycoff 2a site) in the octahedral layers. Rietveld refinement gives the lattice parameters of a=b=2.9002(2) Å, c=11.1765(1) Å, and volume=81.413(1) Å³. which are in close to the NM material (Figure S1, Table S3). In this P2 structure, the Mn-O layer is composed of edge-sharing MnO₆ octahedral chains with ABBA-type sequence stacking along c-direction, and sodium ions occupy two different sites between Mn-O layers as shown in Table S2. Both the lengths of a- and c-axes are increased with the substitution of Zn for Mn because of the larger ionic radii of Zn²⁺ (0.74 Å) than that of Mn³⁺ (0.645 Å). High resolution TEM images in Figure 1b and 1c show the highly crystalline layered structure of NZM. The interplanar distance of the NZM lattice are 0.56 and 0.24 nm, corresponding to the (002) and (100) planes, respectively, which are in good agreement with the ex situ HEXRD results. The selected area electron diffraction (SAED) pattern projected along [001] direction in Figure 1e

represents a typical diffraction pattern of a hexagonal layered structure, which is consistent with the XRD and HRTEM results. As seen in the SEM image in Figure 1f, the material exhibits an irregular morphology with micro-size scale, while the energy dispersion spectroscopy (EDS) images in Figure 1g-j clearly reveal the uniform elemental distribution of sodium, zinc, manganese, and oxygen in the NZM particle.

2.2. Electrochemical properties of NZM and NM cathodes

As shown in Figure 2a and b, the NZM and NM electrodes exhibit quite different charge-discharge curves, implying the different electrochemical processes occurring on these two electrodes. For the NZM electrode (Figure 2a), a two-step charge profile is observed with a steeply rising voltage followed with a long voltage plateau above 4.2 V. The initial portion of the charge profile below 4.2 V corresponds to the Na⁺ extraction process with a low capacity contribution of 26 mAh g⁻¹. In this region, the removal of Na⁺ ions must be accompanied with charge compensation of Mn oxidation state. In the continuous charge process, anion redox could occur according to the similar phenomenon in other P2 analogues [32-34] and a total amount of 0.56 Na⁺ are expected to be extracted (corresponding to Na_{0.07}ZnMnO₂). On the other hand, the charge plateau observed at high potential is a fingerprint of anion redox reaction^[32, 30-34] that contributes to most of the detected capacity. [27, 29-34] In the first discharge process, a discharge capacity of 202.4 mAh/g can be achieved, corresponding to 0.79 Na⁺ insertion into the NZM host leading to a formula of Na_{0.86}MnO₂. In contrast, the NM cathode shows a much lower initial charge capacity of 104.6 mAh g⁻¹, corresponding

to only 0.4 Na⁺ extracted from the host (Figure 2b). In this process, all charge can be readily compensated by the oxidation of Mn³⁺ to Mn⁴⁺ without any anionic redox observed. Moreover, the average voltage of NZM electrode (2.63 V) during discharge is much higher than that of NM sample (2.21 V), also consistent well with the expected contribution from the oxygen redox reaction.

The dO/dV curves derived from the charge/discharge profiles clearly show the very distinct sodium storage behavior of the two electrodes (Figure 2c). For the NZM cathode, two dQ/dV redox couples are revealed. The coupled peaks located at about 2 V are due to Mn³⁺/Mn⁴⁺ redox reaction, whereas the other couple at high potential is derived from the $O^{2-}/(O_2)^{n-}$ redox process with a large hysteresis usually observed in many anion-reactive materials.^[27] As expected, the anionic redox peaks are not observed for the NM sample (Figure 2d). Except the major redox peaks of Mn³⁺/Mn⁴⁺ couple, multiple weak peaks are also emerged in the NM dQ/dV curves due to the complicated phase transitions and rearrangements of Na⁺/vacancy in the typical NM material. [32] The strong peaks at high voltage region are most likely resulted from the severe P2-O2 transition of NM material and will be discussed later. It can also be seen that the peak intensities decrease with increasing the charge-discharge cycles, which is derived from the irreversibility of Mn^{3+/4+} in NM material. As showed in Figure 2e, the NZM electrode can keep 67% of its initial capacity after 50 cycles, while the NM electrode remains only 44% of its initial capacity. Indicated by the absence of the weak peaks in Figure 2c, the higher retention of NZM electrode could be ascribed to the inhibition of the phase transitions during the electrochemical process. On the other hand,

the NZM electrode also presents an improved rate capability, exhibiting higher inherent capacities of 192, 173, 160 and 140 mAh g⁻¹ at 20, 50, 100 and 200 mA g⁻¹, respectively, compared to those (i.e., 187, 151, 137 and 125 mAh g⁻¹) of the NM electrode at the same currents. After back to 20 mA g⁻¹, NZM can almost recover its initial capacity and keep stable cycling while the NM material shows a severe capacity fade due to its structural instability.

2.3. Structural evolutions by in situ HEXRD

To reveal the structure evolution during sodiation/de-sodiation processes of the prepared materials, *in situ* HEXRD experiments were performed on both the NZM and NM materials. For the NM electrode, a new O2-type phase appears when charged to 3 V and coexists with the pristine P2-type phase during further charging (Figure S2), indicating a P2-O2 phase transformation occurred in the NM material. Such a phase transition would bring about severe strain in the lattice, which surely deteriorates the structural stability that results in internal stress and cracks over long-term cycling. [35, 36] In a sharp contrast, no significant phase transformation was observed in the NZM electrode during the whole initial cycle as shown in **Figure 3**a-c. All the diffraction peaks of the NZM material can be indexed to the P2-type structure with gradual changes of the peak intensities and peak positions. This suggests a moderate structural evolution without phase transition in the NZM material. The lattice parameters (*a/b*, *c*, and *V*) of the NZM material at different charge/discharge states were extracted from the *in situ* XRD patterns within the initial cycle (Figure 3d and Figure S3). During the charge

process, four different P2-type phases (P2', P2", P2", and P2"" as marked in Figure 3d) appear successively with differently evolved lattice parameters. Since the *c*-spacing in the layered framework is highly correlated to the sodium ions diffusion, the changes of parameter *c* would sensitively induce different electrochemical performance of the NZM electrode. As shown in Figure 3d, the maximum changes of the *c* and *V* are only 0.8% and 1.0%, respectively, during the entire charging process, which is much smaller than those of the previously reported layered cathode materials.^[34] As a result, the present Zn-doping strategy can not only suppress the lattice phase transformations, but also restrain the volume changes during the charge-discharge process, resulting in nearly zero-strain cathode materials for SIBs.

2.4. Electronic structure changes

To further investigate the reactivity of the as-prepared materials, we conducted the *in situ* X-ray absorption spectroscopy (XAS), including X-ray absorption near-edge structure (XANES) and extended X-ray absorption fine structure (EXAFS) experiments, on both the NZM and NM electrodes. As shown in **Figure 4**a, there are three main features containing two pre-edge peaks (P1 and P2), one shoulder peak (A), and a main white-line peak (M) emerged in the Mn *K*-edge XANES spectra, reflecting the electronic structural evolutions during the redox reactions. For the NZM electrode, the intensities of the pre-edge peaks increase during the charge process, which correlates to an increase of structurally disordered degree due to the oxygen reactive redox in the lattice as proved previously.^[37] With Na⁺ inserted back into the NZM framework, the intensities of the pre-edge peaks recover to their original values, indicating the high

reversibility of the Mn redox. However, for the NM material, the interval between P1 and P2 decreases (Figure S4a-c), indicating a structural change in the NM material consistent well with the in situ HEXRD results. On the other hand, the labeled peak A is contributed from the hybridized 4p-3d states. The reduced intensity of the peak A after initial charge implies an increase of Mn 3d states, indicating an electron transfer from 2p of oxygen to 3d states of Mn. For both of the materials, the main peak (M) shifts to higher energy upon initial charge, indicating the oxidation of Mn. And during the subsequent discharge process, the peak M shifts to lower energy region, reflecting the reduced valence of Mn ions. The smaller energy shifts of the peak M in NZM than that in NM prove the higher valence of Mn in the NZM material. The in situ EXAFS spectra of the NZM and NM electrodes during the first one and half cycles are shown in Figure 4d-f and Figure S4d-f, respectively. The peaks at ~1.3 Å and 2.5 Å are corresponding to the Mn-O bonds and Mn-Mn atom pairs, respectively. The position and intensity of the Mn-O bonds change slightly, implying stable local MnO₆ octahedra in the NZM lattice. In a sharp contrast, the EXAFS peak intensities for the NM material vary dramatically. It is widely known that the peak intensity of EXAFS adopting local octahedral ligand environment is mainly contributed from the coordination number of the central element (here is Mn), structural disorder, amplitude reduction factor, etc. The obvious changes in the EXAFS peak intensity of NM suggest the significant structural evolutions during cycling, which is well consistent with the in situ HEXRD results.

Besides, the charge compensation mechanism during the first cycle for high-capacity NZM electrode is further investigated by ex situ X-ray photoelectron spectrums (XPS) as shown in Figure 4g-i. For the NZM material, two O²⁻ peaks belonging to lattice oxygen (529.5 eV) and oxygenated deposited species (532 eV) can be observed. After being charged to 4.5 V, a new component with a lower electronic density appears at 530.5 eV, suggesting the existence of O⁻/O₂²⁻ species or other under coordinated oxygen atoms. [38] This peak disappears in the discharged electrode, indicating the reversible reduction of O. This phenomenon is not observed in the NM electrode (see Figure S4gi), which demonstrates the different charge compensation mechanisms in the NZM and NM materials, and these phenomena are in good accordance with the *in situ* XAS results. Furthermore, the electrochemical impedance spectroscopy (EIS) and the fitted parameters are displayed in Figure S5 and Table S4-5. The charge transfer resistance increased obviously during the long charging plateau region for NZM, originating from the reactions on surface and structural reorganization. [31] Such significant increase is not observed for the NM material, also suggesting the different reaction processes of these two materials upon initial charge.

Operando mass spectrometer (MS) is employed to explore the oxygen loss in the first charge process of NZM as displayed in Figure S6. No O₂ gas release is detected during the whole cycle except for a small amount of CO₂. According to an earlier study, the release of CO₂ below 4 V and 4.5 V can be ascribed to the decomposition of resident Na₂CO₃ and the oxidation of electrolyte at the end of charge, respectively.^[30] This indicates no oxygen loss from the NZM lattice during the charging process, and that

the valent orbitals of Zn^{2+} can remain above the π^* orbital of the O_2^{2-} , thus avoiding O_2 release.^[27] Moreover, the stable anionic sublattice without any oxygen loss should be the main reason for the stability of the NZM structure.

2.5. Electrochemical reaction mechanism

According to previous reports, the oxygen redox activity can occur in the Nadeficient P-type layered oxide $Na_xM_yMn_{1-y}O_2$ (M = Li, Mg, Ni, etc.), but the correlation among the M content, structure stability and the extent of oxygen involvement have never been clearly revealed. To build such a correlation, we designed and successfully synthesized a series of Zn-substituted Na_{2/3}Zn_xMn_{1-x}O₂ materials with x = 0, 0.1, 0.15, 0.2, 0.25, 0.28, 0.3, respectively. The XRD results (Figure S7) reveal that the ZnO impurities appear only when Zn content arrives at a high value above 0.28, although the P2-type structure still dominates the NZM lattice. Thus, we choose the $Na_{2/3}Zn_xMn_{1-x}O_2$ (x = 0, 0.1, 0.15, 0.2, 0.25) materials to study the effect of Zn content on their structural stability. As discussed above, unobvious phase transition and ultralow lattice strain are observed in the NZM lattice as 25% Mn ions are substituted by Zn. We also conduct ex situ XRD experiments on the Na_{2/3}Zn_{0.2}Mn_{0.8}O₂ electrode with low-content Zn substitution at charged state. As clearly shown in Figure S8, a new O2 phase appears in the XRD pattern, indicating the occurrence of P2-O2 transition in $Na_{2/3}Zn_{0.2}Mn_{0.8}O_2$, which is similar to the previous observation on Na_{2/3}Mn_{7/9}Zn_{2/9}O₂. ^[22] This further confirms that higher substituting content of Zn contributes greatly to the structure stability. This phenomenon could be possibly explained by the more significant oxygen redox reactivity induced by high Zn content

thus as to cause less Mn⁴⁺ reduced to Mn³⁺. Therefore, the Jahn-Teller effect of Mn³⁺ can be effectively suppressed to achieve low lattice strain of the lattice. Here we try to separate the capacities from O and Mn redox reactions semi-quantitatively. According to the dQ/dV curves of the electrodes with different Zn contents in **Figure 5**a, similar peaks representing the oxygen reaction arise even with low Zn content of 0.1. We carefully recognize the starts and ends of the reduction peaks, and then separate the capacity within the corresponding voltage range as the capacity contributed by O, denoted with red line in Figure 5b. Accordingly, the rest of the capacity is therefore considered as the contribution of Mn redox. As shown in Figure 5c and 5d, there is an obvious linear relationship between the capacity of O and Zn contents, so as the capacity of Mn and Zn contents. Based on these results, the O redox contributes a capacity of 132.6 mAh g⁻¹ in Na_{2/3}Zn_{0.25}Mn_{0.75}O₂, suggesting that 26% of the lattice O takes part in the first charge/discharge process. This result is close to the O atomic percentage of O₂ⁿ⁻ species calculated by fitting the XPS peaks (30%).

To further confirm the effect of Zn content on structural stability, the cyclability of the NZM materials with different Zn contents were compared in Figure S9. After 50 cycles, the capacity retentions were 44%, 54%, 63%, 66% and 67% for x=0, 0.1, 0.15, 0.2 and 0.25, respectively, which agrees well with the results above.

2.6. Structural stability in air

The structural instability in air atmosphere is a serious problem hindering the applications of layered cathode materials. To investigate the air sensitivity of these materials, we first exposed the NZM powders and electrodes to ambient air and then

recorded the XRD patterns of them after exposure for 3 days, 30 days and heated at 80°C, respectively. For the NM powders (Figure S10d and e), the air exposure for 30 days leads to a hydrated phase emerging to prevail over the pristine P2 structure, and even after 3 days' exposure, a certain amount of hydrated phase still emerges. In general, the electrode is more sensitive to air than the powders. After exposure for 3 days, the hydrated phase arises apparently in the NM electrode, and the P2 phase disappears entirely after 30 days. In contrast, the Zn-substituted sample exhibits much better structural stability in air. Even after 30 days' exposure, the NZM powders remain single P2 phase without any impurity. However, the NZM electrode seems to be stable in 3 days and then still suffers from water intercalation due to the air moisture after 30 days. To further evaluate the reversibility of the water intercalation reaction, we also collected the XRD patterns after a heating procedure to 80 °C, aiming to remove the unfavorable hydrated phase. As shown in Figure S10a and b, the NZM electrode can reversibly recover to its P2 phase after heating, demonstrating a good thermal reversibility. However, for the NM sample, the hydrated phase is partially removed, leading to a coexistence of P2 phase and hydrated phase. We also compare the electrochemical performance of the electrodes after exposures and the results are displayed in Figure S10c and f. The NZM and NM samples can respectively deliver an initial capacity of 202.4 and 203.5 mAh g⁻¹, indicating the water intercalation has no obvious impact on the initial capacity. Even a higher capacity is achieved for the NM sample due to the larger d-space of the hydrated phase that allows Na⁺ to intercalate reversibly. After 20 cycles, the NZM sample retains a capacity of 155.3 mAh g⁻¹. By contrast, a sharp drop

of capacity to 129.9 mAh g⁻¹ is observed for the NM sample, suggesting the structure and performance are inevitably destroyed by the intercalated water. Therefore, we can conclude that the Zn-substituted material exhibits a better structural stability in air than the pristine one, due to the strong interaction between Zn and O.

3. Conclusion

To summarize, we have successfully synthesized an ultra-low strain Zn-substituted P2-type Na_{2/3}Zn_{0.25}Mn_{0.75}O₂ as high performance SIB cathode. In the sodiation/desodiation process, this material exhibits an ultra-low lattice strain extending along *c*-direction (0.8%) that terminates with a small change in volume (1.0%). It suggests that Zn substituting can effectively trigger the reversible oxygen redox activity in P2-type Na_{2/3}MnO₂, which supplements and partly supplants the Mn⁴⁺/³⁺ redox capacity. In this way, the Jahn-Teller octahedral distortion of Mn³⁺ are suppressed and therefore the P2-O2 lattice phase transition is inhibited. Furthermore, the close coupling between Zn concentration and the redox degree of oxygen in the charge/discharge process is clearly revealed. This work provides an inspiring example that we can quantificationally tune the content of the substituted component to achieve highly stable structure as well as highly reversible anionic redox capacity.

4. Experimental Section

Materials Synthesis: Na_{2/3}Zn_xMn_{1-x}O₂ materials were synthesized by a simple solidstate method. Stoichiometric amounts of Na₂CO₃, ZnO, and Mn₂O₃ were thoroughly

mixed by a mortar and pestle and then pressed into pellets. The precursor pellets were calcined at 800 °C in a muffle furnace in air.

Materials Characterization: X - ray diffraction (XRD) patterns were recorded on a Rigaku SmartLab 9kW diffractometer operated at 45 kV, 200 mA for Cu Kα (λ = 1.5406 Å), the data was collected in 2 θ range of 10-80° with a scan speed of 3° /min and a step size of 0.01° at ambient temperature and pressure. SEM and TEM images were taken with a field - emission scanning electron microscope (FE - SEM, ZEISS Merlin Compact VP, Germany; EDS, Oxford Instruments Link ISIS) and transmission electron microscope (JEM-2010FEF, Japan). XPS was collected by a Thermo Fisher ESCALAB 250Xi using monochromic Al Kα X-ray source. ICP-OES was performed on Optima 5300DV.

Electrochemical measurement: The electrochemical properties were tested in 2016-type coin cell with Na metal as the counter electrode at room temperature. The working electrodes were made with active material, acetylene black and polyvinylidene difluoride (PVDF) with a weight ratio of 7:2:1. The active mass loading of the electrode is about 1.4 mg cm⁻². Galvanostatic charge—discharge tests were conducted on a battery test system (CT-4008, Neware, Shenzhen Neware Electronics Co., China). CV measurements were recorded with IVIUMnSTAT (N66712) multichannel electrochemical analyser with a scan rate of 0.1 mV/s. EIS data was conducted on Metrohm Autolab potentiostat/galvanostat in the frequency range of 100 kHz to 10 mHz.

Operando MS: The OEMS experiments were carried out in a custom-made cell connected to a gas flow controller and mass spectrometer (modified 5975C mass-selective detector, Agilent)

In situ HEXRD: The in situ synchrotron HEXRD experiments were performed on both NM and NZM materials at beamline 11-ID-C, Advanced Photon Source (APS), Argonne National Laboratory (ANL), with the wavelength of 0.1173 Å. The diffraction patterns were collected at each state with 30 s exposure time following with 10 min wait time for the next scan to avoid a long time X-ray exposure that may induce any potential negative impact on the samples. Each diffraction pattern was fitted with hexagonal structure (P63/mmc symmetry) using FullProf Suite package to obtain the lattice parameters.

In situ XAS: The *in situ* XAS, including XANES and EXAFS, experiments were conducted at beamline 20-BM-B, APS. The experiments were performed using transmission mode across Mn (6539 eV) K-edge for NM and NZM electrodes. The XAS data were analyzed by Athena software. The mass loading of active material is about 6 mg cm⁻² for these *in-situ* experiments.

Supporting Information

Supporting Information is available from the Wiley Online Library or from the author.

Acknowledgements

This research was financially funded by the National Nature Science Foundation of China (Nos. 21673165 and 21972108), National Key R&D Program of China (No.

2016YFB0901500) and supercomputing system in the Supercomputing Center of Wuhan University. Q. Liu acknowledges the supports by the Technology and Innovation Commission under grant JCYJ20180507181806316, the City University of Hong Kong under project Fundamental Investigation of Phase Transformative Materials for Energy Application (Project No. 9610399), and the Shenzhen Research Institute, City University of Hong Kong. This research used resources of the Advanced Photon Source, a U.S. Department of Energy (DOE) Office of Science User Facility operated for the DOE Office of Science by Argonne National Laboratory under Contract No. DE-AC02-06CH11357.

Received: ((will be filled in by the editorial staff))

Revised: ((will be filled in by the editorial staff))

Published online: ((will be filled in by the editorial staff))

References

- [1] C. Delmas, Adv. Energy Mater. **2018**, 8, 1703137.
- [2] C. Fang, Y. Huang, W. Zhang, J. Han, Z. Deng, Y. Cao, H. Yang, *Adv. Energy Mater.* **2016**, *6*, 1501727.
- [3] J. Y. Hwang, S. T. Myung, Y. K. Sun, Chem. Soc. Rev. 2017, 46, 3529.
- [4] Q. Liu, Z. Hu, M. Z. Chen, C. Zou, H. L. Jin, S. Wang, S.L. Chou, S.X. Dou, Small 2019, 15, 1805381.
- [5] M. Z. Chen, Q. Liu, S.W. Wang, E.H. Wang, X. D. Guo, S.L. Chou, Adv. Energy Mater. 2019, 9, 1803609.
- [6] Y. J. Fang, L.F. Xiao, Z. X. Chen, X. P. Ai, H. X. Yang, Y. L. Cao, *Electrochem. Energ. Rev.* **2018**, *1*, 294–323.

- [7] Y. J. Fang, Z. X. Chen, X. P. Ai, H. X. Yang, Y. L. Cao, Acta Phys. -Chim. Sin. 2017, 33, 131 -134.
- [8] T. Zhu, P. Hu, X. Wang, Z. Liu, W. Luo, K. A. Owusu, W. Cao, C. Shi, J. Li, L. Zhou, L. Mai, Adv. Energy Mater. 2019, 9, 1803436.
- [9] B. Sun, P. Xiong, U. Maitra, D. Langsdorf, K. Yan, C. Wang, J. Janek, D. Schröder, G. Wang, Adv. Mater. 2019, 1903891.
- [10] X. Guo, J. Zhang, J. Song, W. Wu, H. Liu, G. Wang, *Energy Storage Materials* **2018**, *14*, 306.
- [11] A. Mukhopadhyay, B. W. Sheldon, *Prog. Mater Sci.* **2014**, *63*, 58.
- [12] M. H. Han, E. Gonzalo, G. Singh, T. Rojo, Energy Environ. Sci. 2015, 8, 81.
- [13] C. Delmas, C. Fouassier, P. Hagenmuller, *Physica B+C* **1980**, *99*, 81.
- [14] X. Ma, H. Chen, G. Ceder, J Electrochem Soc 2011, 158, A1307.
- [15] S. Kumakura, Y. Tahara, S. Sato, K. Kubota, S. Komaba, *Chem. Mater.* **2017**, 29, 8958.
- [16] J. Billaud, G. Singh, A. R. Armstrong, E. Gonzalo, V. Roddatis, M. Armand, T. Rojo, P. G. Bruce, *Energy Environ. Sci.* 2014, 7, 1387.
- [17] A. Caballero, L. Hernan, J. Morales, L. Sanchez, J. S. Pena, M. A. G. Aranda, *J. Mater. Chem.* **2002**, *12*, 1142.
- [18] N. Yabuuchi, K. Kubota, M. Dahbi, S. Komaba, Chem. Rev. 2014, 114, 11636.
- [19] N. Yabuuchi, M. Kajiyama, J. Iwatate, H. Nishikawa, S. Hitomi, R. Okuyama, R. Usui, Y. Yamada, S. Komaba, *Nature Mater* 2012, 11, 512.

- [20] H. Wang, B. Yang, X.-Z. Liao, J. Xu, D. Yang, Y.-S. He, Z.-F. Ma, *Electrochim. Acta* **2013**, *113*, 200.
- [21] X. Wang, M. Tamaru, M. Okubo, A. Yamada, *The Journal of Physical Chemistry C* **2013**, *117*, 15545.
- [22] N. Yabuuchi, R. Hara, K. Kubota, J. Paulsen, S. Kumakura, S. Komaba, *J. Mater. Chem. A* **2014**, 2, 16851.
- [23] J. Zhao, J. Xu, D. H. Lee, N. Dimov, Y. S. Meng, S. Okada, *J Power Sources* 2014, 264, 235.
- [24] N. Yabuuchi, R. Hara, M. Kajiyama, K. Kubota, T. Ishigaki, A. Hoshikawa, S. Komaba, *Adv. Energy Mater.* **2014**, *4*, 1301453.
- [25] W. M. Dose, N. Sharma, J. C. Pramudita, J. A. Kimpton, E. Gonzalo, M. H. Han,T. Rojo, *Chem. Mater.* **2016**, 28, 6342.
- [26] W. M. Dose, N. Sharma, J. C. Pramudita, H. E. A. Brand, E. Gonzalo, T. Rojo, Chem. Mater. 2017, 29, 7416.
- [27] X. Bai, M. Sathiya, B. Mendoza-Sánchez, A. Iadecola, J. Vergnet, R. Dedryvère,
 M. Saubanère, A. M. Abakumov, P. Rozier, J.-M. Tarascon, *Adv. Energy Mater.* 2018,
 8, 1802379.
- [28] X. Rong, E. Hu, Y. Lu, F. Meng, C. Zhao, X. Wang, Q. Zhang, X. Yu, L. Gu, Y.-S. Hu, H. Li, X. Huang, X.-Q. Yang, C. Delmas, L. Chen, *Joule* 2018, 3, 503.
- [29] R. J. Clément, J. Billaud, A. Robert Armstrong, G. Singh, T. Rojo, P. G. Bruce, C.P. Grey, *Energy Environ. Sci.* 2016, 9, 3240.

- [30] U. Maitra, R. A. House, J. W. Somerville, N. Tapia-Ruiz, J. G. Lozano, N. Guerrini, R. Hao, K. Luo, L. Jin, M. A. Perez-Osorio, F. Massel, D. M. Pickup, S. Ramos, X. Lu, D. E. McNally, A. V. Chadwick, F. Giustino, T. Schmitt, L. C. Duda, M. R. Roberts, P. G. Bruce, *Nat Chem* **2018**, *10*, 288.
- [31] C. Ma, J. Alvarado, J. Xu, R. J. Clement, M. Kodur, W. Tong, C. P. Grey, Y. S. Meng, J. Am. Chem. Soc. 2017, 139, 4835.
- [32] Y. Li, X. Wang, Y. Gao, Q. Zhang, G. Tan, Q. Kong, S. Bak, G. Lu, X.-Q. Yang,L. Gu, J. Lu, K. Amine, Z. Wang, L. Chen, *Adv. Energy Mater.*, 2019, 9, 1803087.
- [33] B. Mortemard de Boisse, S.-i. Nishimura, E. Watanabe, L. Lander, A. Tsuchimoto,
 J. Kikkawa, E. Kobayashi, D. Asakura, M. Okubo, A. Yamada, *Adv. Energy Mater*.
 2018, 8, 1800409.
- [34] S. Kumakura, Y. Tahara, K. Kubota, K. Chihara, S. Komaba, Angew. Chem. Int. Ed. 2016, 55, 12760.
- [35] A. O. Kondrakov, A. Schmidt, J. Xu, H. Geßwein, R. Mönig, P. Hartmann, H. Sommer, T. Brezesinski, J. Janek, *The Journal of Physical Chemistry C* **2017**, *121*, 3286.
- [36] P. Yan, J. Zheng, J. Liu, B. Wang, X. Cheng, Y. Zhang, X. Sun, C. Wang, J.-G. Zhang, *Nature Energy* **2018**, *3*, 600.
- [37] T. Okumura, Y. Yamaguchi, H. Kobayashi, *Physical Chemistry Chemical Physics* **2016**, *18*, 17827.
- [38] M. Sathiya, K. Ramesha, G. Rousse, D. Foix, D. Gonbeau, A. S. Prakash, M. L. Doublet, K. Hemalatha, J. M. Tarascon, *Chem. Mater.* **2013**, *25*, 1121.

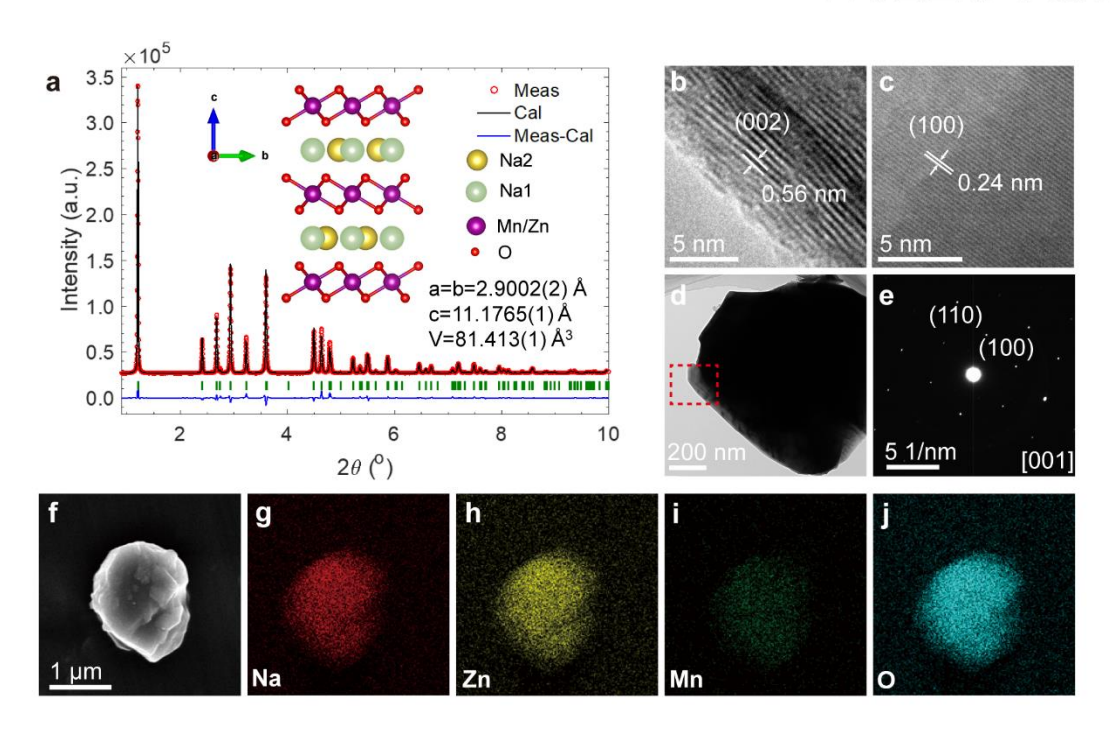


Figure 1. Crystal structure of the as-prepared NZM. (a). Rietveld refinement of the HEXRD pattern of the NZM material. The red circles and the black line represent the experimental and calculated diffraction patterns, respectively, and the blue line shows the difference between the experimental and calculated patterns. The refined structure, illustrated inset, is in $P6_3/mmc$ space group symmetry. Lattice parameters a(b), c and V are also shown in Figure 1a. TEM images (b, c), SAED pattern (d, f) and element mapping (f-j) of NZM material.

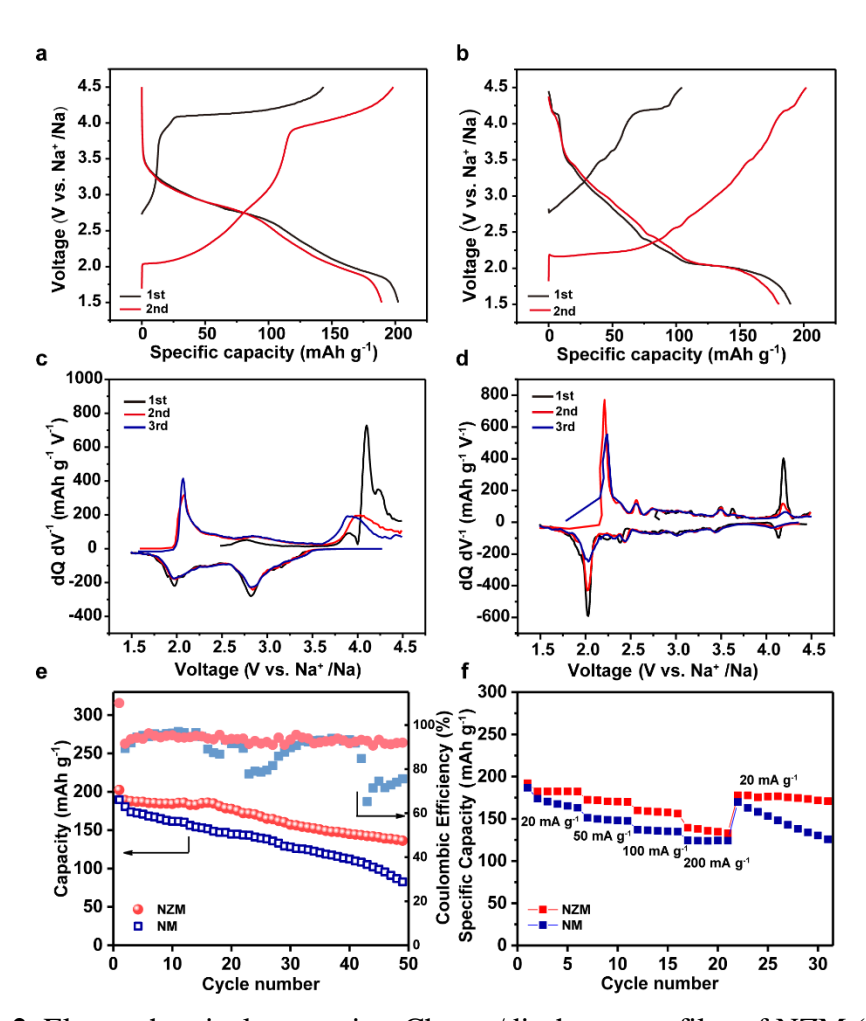


Figure 2. Electrochemical properties. Charge/discharge profiles of NZM (a) and NM (b) at 20 mA $\rm g^{-1}$; dQ/dV curves of NZM (c) and NM (d); Cyclability at 20 mA $\rm g^{-1}$ (e) and rate capability (f) of the NZM and NM materials. The voltage range is within 1.5-4.5 V.

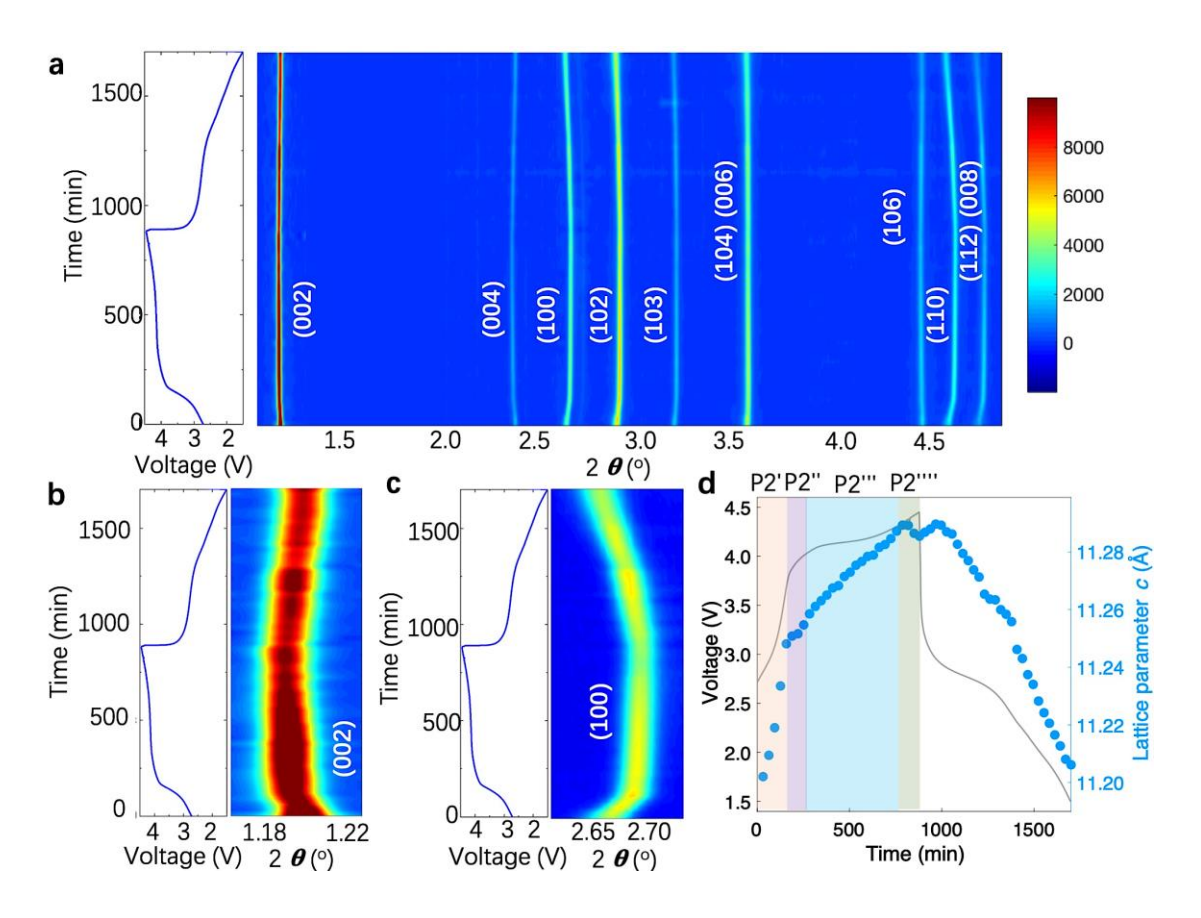


Figure 3. *In situ* HEXRD characterization of the structural evolution of NZM electrode. (a) Contour plot of the *in situ* HEXRD patterns during the initial cycle along with the charge-discharge profiles. The intensity colormap for the contour plot is illustrated on the right. Enlarged contour plots of (b) (002) and (c) (100) peaks in Figure a. (d) The corresponding lattice parameter c evolutions, obtained by refining in situ XRD patterns with $P6_3/mmc$ structural model, during charge and discharge processes. The distorted P2-type phases with various lattice parameters are marked by different color areas.

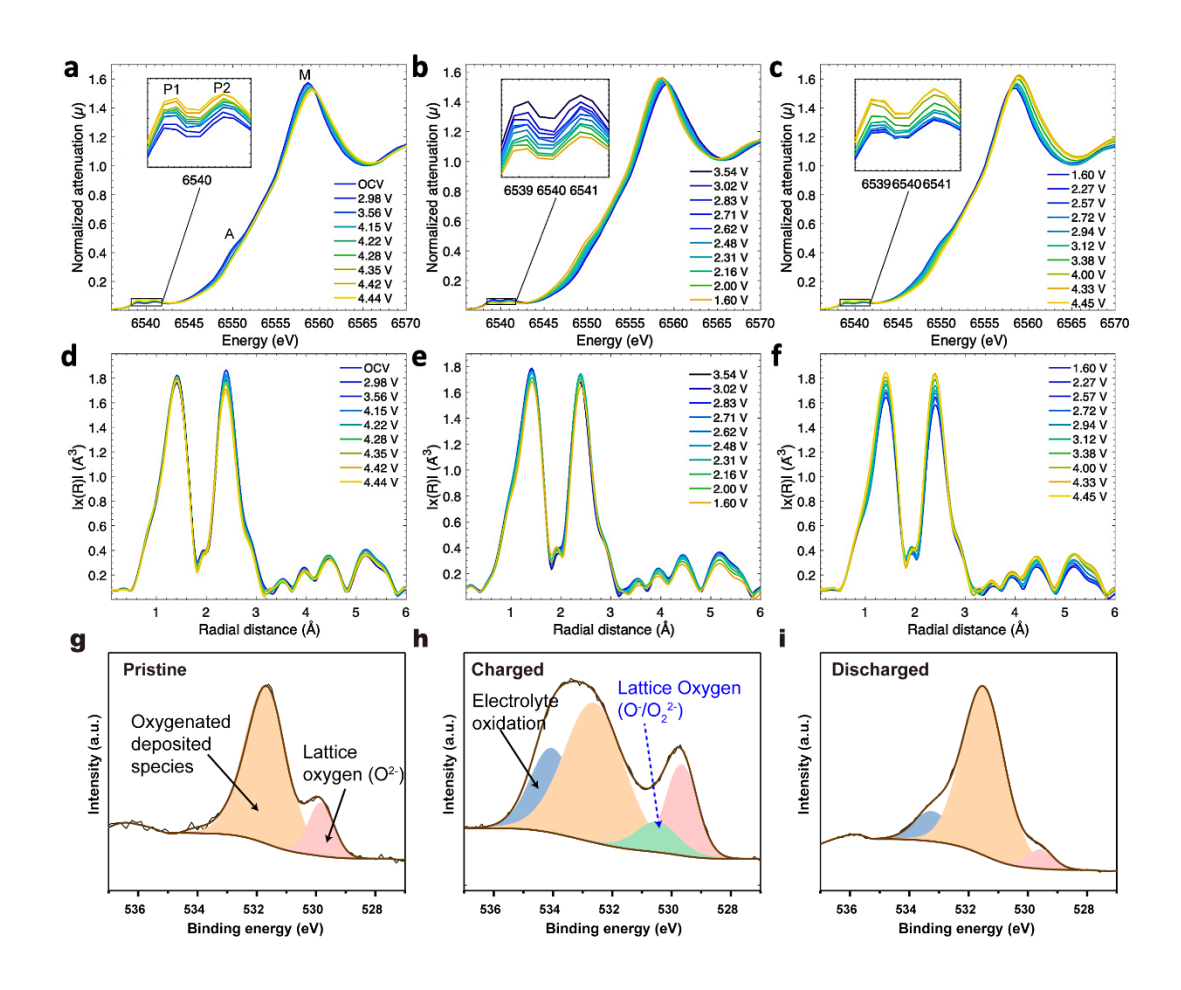


Figure 4. *In situ* XAS experiments performed on NZM electrode at Mn K-edge and ex *situ* XPS analysis of the samples. (a-c) The XANES and (d-f) the Fourier transformed EXAFS of NZM electrode during the first charge, first discharge, and second charge processes, respectively. (g-i) XPS O 1s spectra of NZM samples, the red, orange, green and blue area represent lattice oxygen, oxygenated deposited species, O⁻/O₂²⁻ species and electrolyte oxidation species, respectively.

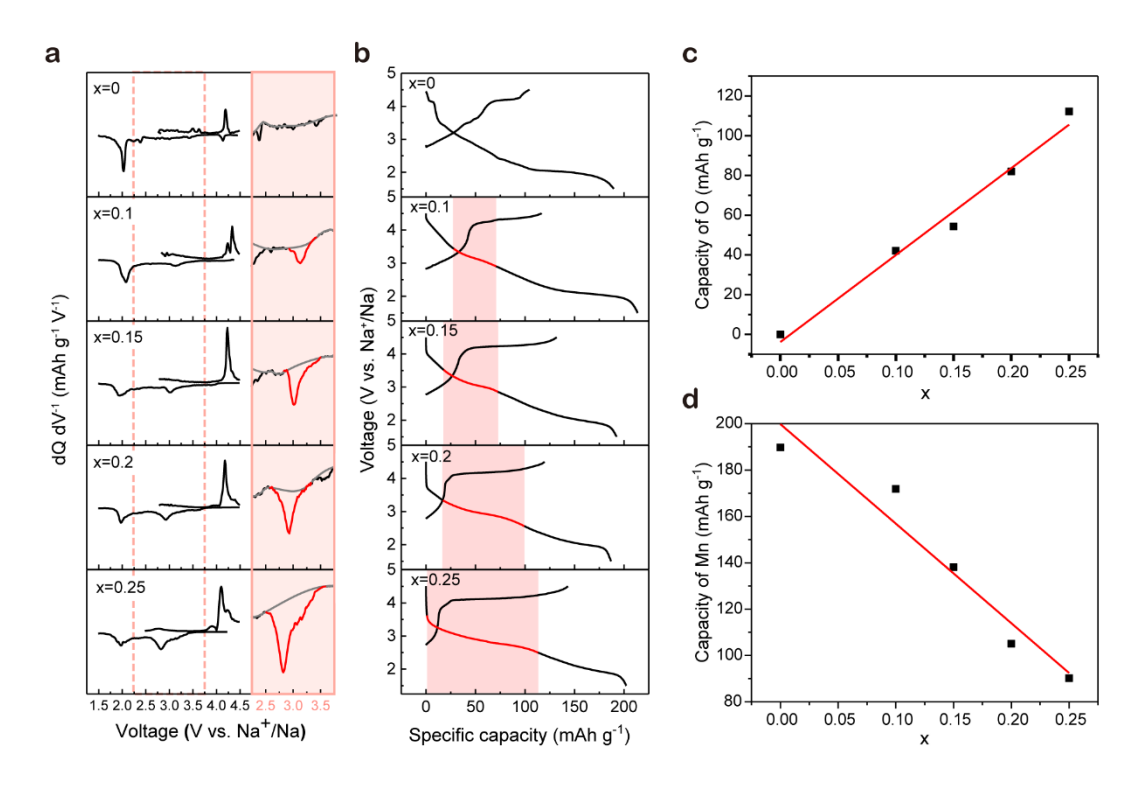


Figure 5. dQ/dV curves (a) and charge/discharge curves (b) of Na_{2/3}Zn_xMn_{1-x}O₂ (x = 0, 0.1, 0.15, 0.2, 0.25) at 20 mA g⁻¹ in 4.5-1.5 V and the relationships regarding Zn content with the capacities of O (c) and Mn (d) redox reactions, respectively.

A high-concentration Zn-substituted P2-type is found to exhibit ultra-low strain characteristic as a high-performance SIBs cathode. In the sodiation/de-sodiation process, this P2-Na_{2/3}Zn_{0.25}Mn_{0.75}O₂ exhibits a near zero strain extending along c-direction (0.8%) and a small change in volume (1.0%), which significantly improves the cycling stability and rate capability of the cathode material.

Keywords: ultralow strain, substitution, phase transition, sodium ion batteries

Yanxia Wang[†], Liguang Wang[†], He Zhu, Jun Chu, Yongjin Fang, Lina Wu, Ling Huang, Yang Ren, Cheng-Jun Sun, Qi Liu^{*}, Xinping Ai, Hanxi Yang, Yuliang Cao^{*}

Ultralow-strain Zn-substituted Layered Oxide Cathode with Suppressed P2-O2 Transition for Stable Sodium Ion Storage

